

Signatures of Wigner molecule formation in interacting Dirac fermion quantum dots

Tomi Paananen¹, Reinhold Egger¹, and Heinz Siedentop²

¹*Institut für Theoretische Physik, Heinrich-Heine-Universität, D-40225 Düsseldorf, Germany*

²*Mathematisches Institut, Ludwigs-Maximilians-Universität München, D-80333 München, Germany*

(Dated: June 24, 2018)

We study N interacting massless Dirac fermions confined in a two-dimensional quantum dot. Physical realizations of this problem include a graphene monolayer and the surface state of a strong topological insulator. We consider both a magnetic confinement and an infinite mass confinement. The ground state energy is computed as a function of the effective interaction parameter α from the Hartree-Fock approximation and, alternatively, by employing the Müller exchange functional. For $N = 2$, we compare those approximations to exact diagonalization results. The Hartree-Fock energies are highly accurate for the most relevant interaction range $\alpha \lesssim 2$, but the Müller functional leads to an unphysical instability when $\alpha \gtrsim 0.756$. Up to 20 particles were studied using Hartree-Fock calculations. Wigner molecule formation was observed for strong but realistic interactions, accompanied by a rich peak structure in the addition energy spectrum.

PACS numbers: 03.65.Pm, 73.22.Pr, 71.15.Rf, 73.21.La

I. INTRODUCTION

Massless two-dimensional (2D) Dirac fermions are of central importance in several condensed matter applications of current interest, in particular for monolayer graphene^{1,2} and for the surface state of a 3D strong topological insulator (TI).^{3,4} These systems offer readily accessible table-top realizations of relativistic quantum physics, where electron-electron interactions are typically much stronger than in atomic physics. Interactions are characterized by an effective fine structure constant α , where for graphene $\alpha \approx 1$ to 2 depending on experimental details,² while in TIs α is probably somewhat smaller due to the large dielectric constant of the relevant thermoelectric materials (for instance, Bi₂Se₃ or Bi₂Te₃).⁵ We here study the problem of N massless 2D Dirac quasi-particles confined to a circular quantum dot of radius R and interacting through the Coulomb potential (with prefactor $\propto \alpha$). Quantum dots formed in 2D semiconductor heterostructures have been studied in much detail over the past two decades, both experimentally⁶ and theoretically.⁷ Given the exceptional properties of Dirac fermions and the unique properties of the underlying materials, it is of considerable practical and fundamental interest to investigate Dirac fermion quantum dots. Since the commonly employed electrostatic gating⁶ is problematic due to the (recently observed⁸) Klein tunneling phenomenon, the question of how to confine Dirac fermions in a controlled manner arises. While quasi-bound states induced by electrostatic potentials have also been studied,^{9–13} we here consider two types of *stable* confinement: (i) an infinite-mass boundary condition^{14–16} on the single-particle wavefunction at $r = R$, and (ii) confinement by a spatially inhomogeneous magnetic field profile.^{17–20} Graphene dots have already been investigated experimentally by several groups,^{21–26} where confinement was so far created lithographically. While this (approximately) corresponds to case (i) above, such a procedure may give rise to uncon-

trolled disorder effects along the boundary, and route (ii) may offer a promising alternative for future experiments, see also Ref. 27. For the TI surface state, we are not aware of experimental reports of quantum dot physics, but confinement should be achievable as well using, e.g., suitably arranged close-by ferromagnetic layers.

On the theoretical side, another difficulty arises from the Dirac nature of the quasi-particles when one attempts to include electron-electron interactions. For the N -particle problem, where a first-quantized formulation generally offers the most natural route,⁷ the problem arises from the unboundedness of the single-particle Dirac Hamiltonian in Eq. (1) below. This causes the Brown-Ravenhall²⁸ “disease:” the unbounded spectrum allows particles to lose arbitrary amounts of energy by transferring their energy in (real) scattering events to other particles. To circumvent this problem, suppose that the chemical potential is located just above the Dirac point. We then follow Sucher²⁹ and confine the Hilbert space to positive-energy eigenstates of the full single-particle problem, i.e., we assume an inert filled Dirac sea. This projection approach has been successfully employed in the same context before,^{19,20} and one can analyze also other values for the chemical potential. The accuracy of this method was carefully assessed in Ref. 19. In short, the presence of a spectral gap due to confinement allows to implement Sucher’s no-pair approximation²⁹ since electron-hole pair excitations neglected in this approach have to overcome the gap.

Below we show and compare results from three different computational approaches. In particular, we perform self-consistent Hartree-Fock (HF) calculations and, in addition, study a similar self-consistent variational procedure using the so-called Müller density matrix functional (replacing the Fock term).^{30,31} In atomic physics applications, the Müller functional is sometimes superior to the HF approach and is valuable because it yields a *lower* bound for the ground-state energy.³¹ We note that HF calculations for graphene dots with infinite-mass confine-

ment have also been carried out by other groups.^{32,33} While the HF approximation is known to provide an upper bound for the exact (within Sucher's projection approach) ground-state energy,²⁰ the Müller functional is again expected to generate a variational lower bound. We will compare results from those two approaches to exact diagonalization computations for $N = 2$ interacting Dirac quasi-particles. The model and those three numerical approaches are described in Sec. II, while the comparison for $N = 2$ can be found in Sec. III. As expected, the exact results are always bracketed by the results obtained from the Müller functional and under the HF approximation. However, within the range $\alpha \leq 2$ studied in this work, we find that the HF results are much closer to the exact results and provide a rather accurate approximation. However, results based on the Müller functional show an unphysical divergence when $\alpha \gtrsim 0.756$, and are less accurate than the HF results for small α . (Of course, for $\alpha \rightarrow 0$, all three methods recover the correct noninteracting results.) Having established the HF approach as highly accurate approach for $\alpha \leq 2$ and $N = 2$, we continue in Sec. IV with a presentation of HF results for $N > 2$ Dirac particles in a quantum dot with infinite-mass confinement. Besides the ground-state energy, we study various physical observables like the particle density or the spin density. Our results suggest that in a confined geometry Dirac particles can form a "Wigner molecule" as previously discussed for Schrödinger particles in semiconductor dots.^{7,34-36} When the Coulomb interactions dominate over the kinetic energy, a Wigner crystal can be formed where electrons spontaneously order in a crystalline structure. The presence of a confining potential makes this Wigner crystallization more favorable,³⁵ and although no Wigner crystal is expected for bulk graphene,³⁷ we find that the confined geometry allows for a finite-size Wigner "molecule" even for Dirac fermions. The paper concludes with a discussion in Sec. V.

II. MODEL AND COMPUTATIONAL APPROACHES

In this section we discuss the model studied in this work, and address the different calculational schemes employed to study the N -particle problem for interacting Dirac fermions in a quantum dot.

A. Single-particle model

We consider a single species of massless 2D Dirac fermions described by the single-particle Hamiltonian ($-e < 0$ is the electron charge)

$$H_0 = v_F \boldsymbol{\sigma} \cdot \left(\mathbf{p} + \frac{e}{c} \mathbf{A} \right) + M \sigma_3, \quad (1)$$

where $\boldsymbol{\sigma} = (\sigma_1, \sigma_2)$ and the Pauli matrices σ_i refer to the sublattice structure of the honeycomb lattice for

graphene² or to the electronic spin degree of freedom for the TI surface state.³ The Fermi velocity in graphene is $v_F \approx 10^6$ m/s, while the corresponding value for the TI surface state is approximately half this value. A single Dirac cone as in Eq. (1) can be realized for a TI surface,³ but in graphene there generally is a four-fold degeneracy due to the valley and spin degrees of freedom.² For graphene, we then assume a spin- and valley-polarized situation where the single-valley theory [Eq. (1)] gives useful predictions.³⁸ In fact, our basic qualitative conclusion, i.e., Wigner crystallization is possible in graphene dots, is also found from HF calculations including the spin and valley degrees of freedom.³⁹ In addition, we allow for a static vector potential $\mathbf{A}(\mathbf{r})$ corresponding to inhomogeneous magnetic fields or, in the case of graphene, also to strain-induced pseudo-magnetic fields.² Finally, $M(\mathbf{r})$ corresponds to a mass term. In order to form a quantum dot, where Dirac fermions are confined to a bounded spatial region, say, a disk of radius R around the origin, we now consider the two possibilities mentioned in Sec. I. We study circularly symmetric cases, where the total angular momentum operator $J = -i\hbar\partial_\phi + \hbar\sigma_z/2$ is conserved and has eigenvalues $\hbar j$ with half-integer $j \equiv m + 1/2$, $m \in \mathbb{Z}$. Single-particle solutions to $H_0\psi = E\psi$ can then be written as

$$\psi_m(r, \phi) = e^{im\phi} \begin{pmatrix} \psi_{1,m}(r) \\ ie^{i\phi}\psi_{2,m}(r) \end{pmatrix}. \quad (2)$$

In what follows, we measure energies (lengths) in units of $\hbar v_F/R$ (R), and we always focus on $E > 0$ solutions.

(i) *Infinite mass confinement.*— A well-known way to describe confinement theoretically is to impose an infinite-mass boundary condition on the wavefunction [Eq. (2)] at $r = 1$, i.e., $M(r < 1) = 0$ and $M(r > 1) \rightarrow \infty$. As shown by Berry and Mondragon,¹⁴ the effect of $M(r)$ in Eq. (1) is then fully captured by the boundary condition

$$\psi_{1,m}(1) = \psi_{2,m}(1), \quad (3)$$

stating that no current flows through the boundary. With the Bessel function J_m , the Dirac equation is solved for $r < 1$ by the *Ansatz*

$$\psi_{1,m}(r) = A J_m(Er), \quad \psi_{2,m}(r) = A J_{m+1}(Er),$$

where the boundary condition (3) yields the energy quantization condition¹⁴

$$J_m(E_{mn}) = J_{m+1}(E_{mn}). \quad (4)$$

This equation has to be solved numerically. (Note again that E is given in units of $\hbar v_F/R$ and r in units of R .) Positive-energy solutions for given m are then labeled by $n \in \mathbb{N}$. We mention in passing that there are no zero-energy solutions.¹⁴ The normalization factor A is

$$A_{mn} = [\pi(J_m^2 - J_{m-1}J_{m+1} + J_{m+1}^2 - J_mJ_{m+2})]^{-1/2}, \quad (5)$$

where all Bessel functions are evaluated at E_{mn} . To summarize, the single-particle solutions ψ_a under a circular infinite-mass confinement are labeled by $a = (m, n)$ with $m \in \mathbb{Z}$ and $n \in \mathbb{N}$. The eigenenergies E_a follow by solving Eq. (4) and the eigenspinor is ($r < 1$)

$$\psi_a(r, \phi) = A_a e^{im\phi} \begin{pmatrix} J_m(E_a r) \\ i e^{i\phi} J_{m+1}(E_a r) \end{pmatrix}. \quad (6)$$

For a detailed discussion of the single-particle spectrum, see Ref. 15.

(ii) *Magnetic confinement.*— A second possibility to confine Dirac quasi-particles is to employ spatially inhomogeneous magnetic fields. This possibility has been explored theoretically before,^{17–20} and we study the simplest case of a piecewise constant magnetic field, $B(r) = B\Theta(r-1)$ with $B > 0$ and the Heaviside step function $\Theta(x)$. The eigenenergies for this single-particle problem can be found numerically and were given in Ref. 20. The spectrum contains “dot states”, with probability density concentrated in the disk region $r < 1$, plus relativistic bulk Landau states for $r > 1$. The Landau states are weakly perturbed by the presence of the dimensionless “missing flux” parameter $\delta := R^2/2\ell^2$, where $\ell := \sqrt{c/eB}$ is the magnetic length. Because of this perturbation, Landau level energies are slightly shifted away from their standard bulk value, but dot states can be clearly distinguished in the single-particle spectrum. With chemical potential chosen such that all bulk Landau states below the first Landau state, $E^{(1)} := \sqrt{2}R/\ell$

(in units of $\hbar v_F/R$), are filled, the relevant dot states are in the window $0 < E_a < E^{(1)}$. All eigenstates can again be labeled by $a = (m, n)$, i.e., using angular momentum $j = m + 1/2$ and the index $n \in \mathbb{N}$. For given missing flux δ , there are $N_b(\delta)$ dot states, where N_b increases with increasing δ , see Ref. 20. The N -particle problem can then be studied for $N \leq N_b(\delta)$ only. In fact, due to the repulsive interactions, the maximum number of bound electrons may be lowered even further.²⁰ For the infinite-mass confinement [case (i)], there is no constraint on the number of particles held by the dot.

We now add electron-electron interactions to the N -particle problem. The Coulomb interaction matrix elements are given in terms of the eigenspinors ψ_a ,

$$V_{aa'b'b} := \alpha \int \frac{d\mathbf{r}d\mathbf{r}'}{|\mathbf{r} - \mathbf{r}'|} (\psi_a^\dagger \cdot \psi_b)(\mathbf{r}) (\psi_{a'}^\dagger \cdot \psi_{b'}) (\mathbf{r}'), \quad (7)$$

with $V_{a'abb'} = V_{aa'b'b}$. Due to total angular momentum conservation, only matrix elements with $m_a + m_{a'} = m_b + m_{b'}$ do not vanish. Interaction matrix elements with large momentum exchange $k = m_b - m_a$ ($k \in \mathbb{Z}$) are numerically small,¹⁹ but all possible values of k (for a chosen basis size) are taken into account below. For the magnetic dot [case (ii)], the matrix elements (7) are most conveniently evaluated by expanding ψ_a in conventional relativistic Landau level states.²⁰ For the infinite-mass confinement [case (i)], after inserting Eq. (6) into Eq. (7), some algebra [cf. also Appendix B of Ref. 20] yields

$$\begin{aligned} V_{aa'b'b} &= (4\pi)^2 \alpha A_a A_{a'} A_{b'} A_b \sum_{l=0}^{\infty} C_{k,l} \int_0^1 dr r^{-l} (J_{m_a}(E_a r) J_{m_b}(E_b r) + J_{m_a+1}(E_a r) J_{m_b+1}(E_b r)) \\ &\times \int_0^r dr' (r')^{l+1} (J_{m_{a'}}(E_{a'} r') J_{m_{b'}}(E_{b'} r') + J_{m_{a'}+1}(E_{a'} r') J_{m_{b'}+1}(E_{b'} r')). \end{aligned} \quad (8)$$

The coefficient $C_{k,l}$ vanishes when $l + |k|$ is odd or when $l < |k|$. For $k = l = 0$, we have $C_{k,l} = 1/2$. In all remaining cases, we obtain

$$C_{k,l} = \frac{(2l-1)!!}{2^{l+1}l!} \prod_{n=1}^{(l+|k|)/2} \frac{(n-1/2)(n-l-1)}{n(n-l-1/2)}.$$

Equation (8) is then evaluated by numerical integration routines and yields the interaction matrix elements.

B. Numerical approaches

Next, we briefly describe three different numerical approaches to obtain the ground-state energy for a quantum dot containing N Dirac fermions, namely HF simulations, the Müller density matrix formulation, and exact

diagonalization (for $N = 2$). In order to have a well-defined many-body problem, we follow Sucher²⁹ and restrict ourselves to the projected single-particle space, i.e., we assume an inert filled Dirac sea. Hence summations over $a = (m, n)$ will only include positive-energy single-particle solutions ($E_a > 0$). In the numerical calculations, the basis size (i.e., the number K of single-particle orbitals spanning the Hilbert space) was always chosen sufficiently large to ensure convergence. Failure to converge indicates an instability of the method, as we will see in the case of the Müller functional for strong interactions.

First, the Hartree-Fock approach amounts to the self-

consistent minimization of the functional

$$E_{\text{HF}}[\gamma] = \sum_a E_a \gamma_{aa} + \frac{1}{2} \sum_{aa'bb'} (V_{aa'b'b} - V_{aa'bb'}) \gamma_{a'b'} \gamma_{ab}, \quad (9)$$

where the density matrix γ obeys $\gamma^2 = \gamma$ and $\text{tr}(\gamma) = N$. In our case, γ is a real symmetric matrix. The numerical algorithm to obtain the HF ground state is standard and can be found, for instance, in Ref. 20. Second, the Müller density matrix formulation employs a different form for the exchange term, where one minimizes the functional^{30,31}

$$E_{\text{M}}[\gamma] = \sum_a E_a \gamma_{aa} + \frac{1}{2} \sum_{aa'bb'} \left(V_{aa'b'b} \gamma_{a'b'} \gamma_{ab} - V_{aa'bb'} (\gamma^{1/2})_{a'b'} (\gamma^{1/2})_{ab} \right), \quad (10)$$

where γ is again a real symmetric matrix with $\text{tr}(\gamma) = N$, but now $\gamma^2 \leq \gamma$. A stable numerical approach to minimize $E_{\text{M}}[\gamma]$ in Eq. (10), the so-called projected gradient algorithm, has been formulated and tested before.^{40,41} We have employed precisely the same method here. Finally, the exact numerical diagonalization of the full many-body problem is only possible for small particle numbers due to the exponential increase in computational complexity with increasing N . We have therefore carried out exact diagonalization calculations only for $N = 2$ Dirac fermions, primarily to check the accuracy of the two computationally less expensive but approximate alternative approaches. Details of the exact diagonalization approach have been described in Ref. 19.

III. COMPARISON OF METHODS: $N = 2$

In this section, we show and compare the results of the three approaches described in Sec. II for $N = 2$ Dirac fermions. For the infinite-mass confinement case, results for the ground-state density $E(\alpha)$ are shown in Fig. 1. Clearly, the numerically exact result obtained from exact diagonalization is bracketed by the HF prediction from above and by the Müller result from below. The HF approximation provides very accurate estimates for $E(\alpha)$, while the Müller functional is only reliable for very small α . In fact, the application of the Müller functional to the free-space case reveals an intrinsic divergence for strong interactions $\alpha > \alpha_c$, where the critical value is (see Ref. 42, correcting an earlier attempt⁴³)

$$\alpha_c = \frac{2}{y + 1/y} \approx 0.756, \quad y = \frac{\Gamma^4(1/4)}{8\pi^2}. \quad (11)$$

Although this critical value was derived for the case of vanishing magnetic field, we anticipate that it applies also to the confined geometry, with or without magnetic field, since it arises from the fact that both the kinetic energy and the Coulomb singularity scale as inverse length for short distances, i.e., a regular magnetic field is clearly

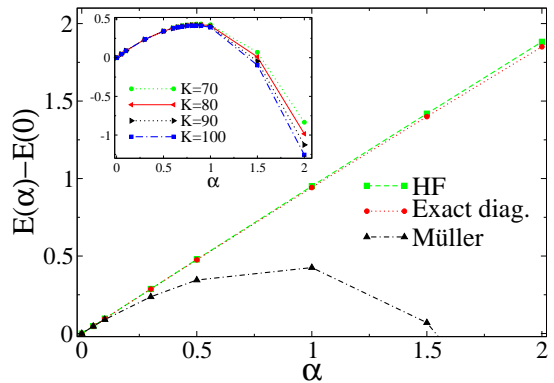


FIG. 1: (color online) Interaction contribution to the ground-state energy, $E(\alpha) - E(0)$ (in units of $\hbar v_F/R$), vs fine structure constant α for the infinite-mass confined dot containing $N = 2$ particles. The main panel shows the results of the three different approaches, see main text. The HF results are very close to the exact diagonalization results, while the Müller functional gives a lower bound. Straight lines are a guide to the eye only. Inset: Same for Müller functional, with different basis size K . Note the absence of convergence for large α .

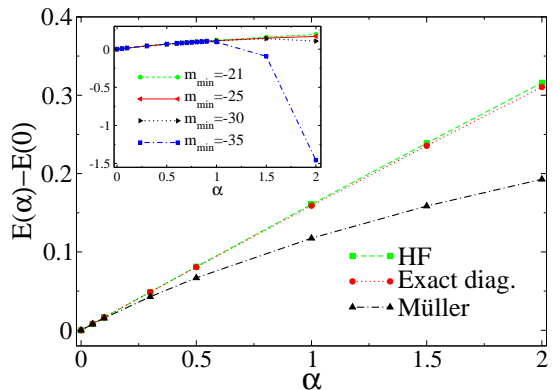


FIG. 2: (color online) Same as Fig. 1 but for the magnetically confined case with $\ell = R$. The basis size K here corresponds to $2|m_{\min}|$.

irrelevant for the singular behavior. (Such a result has recently been established in a related situation.⁴⁴) For $\alpha > \alpha_c$, the exchange part in the Müller functional [Eq. (10)] provides a strong attraction which effectively forces particles to form a droplet. In our case, this singular behavior implies that the “ground-state” energy drops to $-\infty$. In numerical computations, this is reflected by the fact that the energy becomes cutoff-dependent, going to $-\infty$ as the basis size K grows. This phenomenon is clearly visible in the inset of Fig. 1, but a precise comparison of the predicted critical value for α_c [Eq. (11)] with numerics is difficult. This singularity is an unphysical artefact of the Müller density matrix approach and indicates that it is only useful for $\alpha \ll 1$. On the other hand, the HF approximation is very close to the exact value even for $\alpha = 2$.

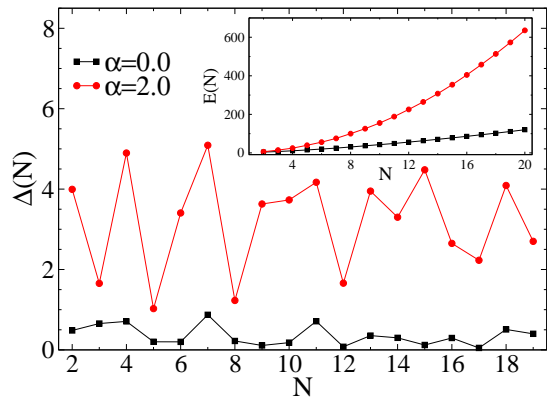


FIG. 3: (color online) HF results for the addition energy $\Delta(N)$ [Eq. (12)] vs particle number N for a dot formed by infinite-mass confinement. Results are shown for $\alpha = 2$ (red circles) and for $\alpha = 0$ (black squares); straight lines are a guide to the eye only. Inset: HF results for the energy $E(N)$ vs N , for the same interaction parameters.

A very similar picture emerges from the corresponding study of the magnetically confined dot, see Fig. 2. In both cases and for all $\alpha \leq 2$, the interaction energy obtained under the HF approximation is less than 1% above the corresponding exact value. In the remainder of the paper, we will then study $N > 2$ particles using the HF approach. We have compared the results of the Müller functional for $N > 2$ to the corresponding HF results as well, and with increasing N they come closer. Hence we expect that the relative accuracy of the HF results (at the least) does not deteriorate for $N > 2$.

IV. HARTREE-FOCK RESULTS FOR $N > 2$ PARTICLES

In the previous section, we have established that HF calculations are able to provide very accurate estimates for the ground-state energy of Dirac fermions in a circular quantum dot. In this section, we describe the results of our HF calculations for up to $N = 20$ particles. For clarity, we focus on the infinite-mass confinement case, but qualitatively similar results were also found for the magnetic confinement.

Figure 3 shows HF results for the N -dependent addition energy,

$$\Delta(N) := E(N+1) + E(N-1) - 2E(N), \quad (12)$$

both for $\alpha = 2$ and for the noninteracting case ($\alpha = 0$). The HF ground-state energy $E(N)$ obtained from our self-consistent numerical calculation is shown in the inset of Fig. 3. A peak in the addition energy for some N implies a higher stability of the N -particle dot. In

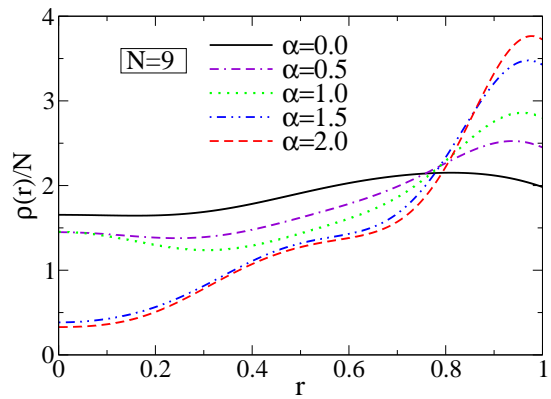


FIG. 4: (color online) HF results for the radial density profile $\rho(r)$ vs r for $N = 9$ particles with several α .

analogy to atomic and nuclear physics, this N is often referred to as “magic number.”⁷ While already the non-interacting dot has some structure in the addition energy spectrum (due to the single-particle spectrum), e.g., the small peaks at $N = 7$ and $N = 11$ visible in Fig. 3, the interacting case is characterized by more pronounced features. For $\alpha = 2$, we observe clear peaks, see Fig. 3, corresponding to the magic numbers $N = 4, 7, 11, 13, 15$ and 18. Although some of these numbers coincide with the noninteracting ones, it is evident that the addition energy spectrum is drastically changed by electron-electron interactions in such a finite-size system.

The resulting ground-state density $\rho(\mathbf{r})$ is rotationally invariant and can therefore be analyzed in terms of the angular-averaged density $\rho(r)$, which is normalized as $\int_0^1 r dr \rho(r) = N$. Figure 4 shows HF results for the density $\rho(r)$ for $N = 9$ and several α . In the non-interacting case ($\alpha = 0$), the density profile is rather smooth, but with increasing α the particles are pushed towards the boundary and form a ring. When comparing the shoulder-like feature apparent in Fig. 4 (around $r \approx 0.5$) to the corresponding correlation plot (see below), we find that no significant particle weight is contained in the shoulder, i.e., with high probability all particles are close to the boundary. For $N = 19$ particles, a richer structure emerges, see Fig. 5, with three different spatial “shells” emerging for strong interactions. In particular, by integrating over the shown density curve, we find that one particle is located near the origin, three particles are contained in a second shell around $r \approx 0.45$, and the remaining 15 particles are close to the boundary.

To obtain more detailed insight we next study the density-density correlation function

$$g(\mathbf{r}, \mathbf{r}') = \langle \rho(\mathbf{r}) \rho(\mathbf{r}') \rangle, \quad (13)$$

where \mathbf{r}' is kept fixed. Monitoring $g(\mathbf{r}, \mathbf{r}')$ as a function of \mathbf{r} , the spatial arrangement of the particles in the dot can be revealed.

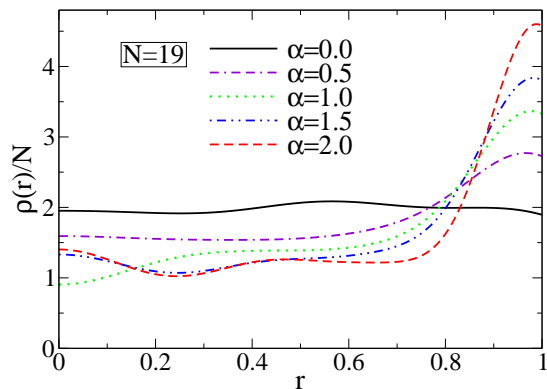


FIG. 5: (color online) Same as Fig. 4 but for $N = 19$.

2D correlation plots for $N = 9$ and $N = 19$ (with $\alpha = 2$) are shown in Fig. 6 and Fig. 7, respectively. In these plots, we keep $\mathbf{r}' = (0.95, 0)$ fixed and show the correlations as function of $\mathbf{r} = (x, y)$ within the dot. For $N = 9$, Fig. 6 is consistent with all electrons being arranged equidistantly on a ring close to the boundary. The correlation plot in Fig. 7 for $N = 19$ particles also confirms the conclusions reached from the analysis of the density plot in Fig. 5. The outermost spatial shell (near the boundary) holds 15 particles, a second ring contains 3 particles, and one particle is located at the center. The combined analysis of density and correlation plots for all particle numbers under study, $N \leq 20$, results in the shell filling sequence in Table I.

These observations provide a signature for the onset of Wigner molecule behavior, i.e., we have a finite-size system where Wigner crystallization sets in but quantum fluctuations are still important.^{35,36} In order to compare to the deep Wigner crystallized limit, we now briefly discuss the classical limit (which here is defined by taking the limit $\alpha \rightarrow \infty$), where the electrostatic energy dominates completely and the kinetic energy can be neglected. The repulsive interaction then tries to maximize the distance between particles, leading to the formation of spatial shells. The shell filling sequence for a harmonically confined Wigner molecule (of Schrödinger fermions) is well known,^{7,34,35} and HF calculations have been able to capture the Wigner molecule formation.³⁶ For the 2D circular hard-wall confinement considered here, however, a different shell filling sequence follows by minimization of the classical electrostatic energy $E_c(N)$ with respect to all particle positions $\mathbf{r}_{i=1,\dots,N}$ within the disk ($r_i \leq R = 1$),

$$E_c(N) = \sum_{i < j}^N \frac{\alpha}{|\mathbf{r}_j - \mathbf{r}_i|}. \quad (14)$$

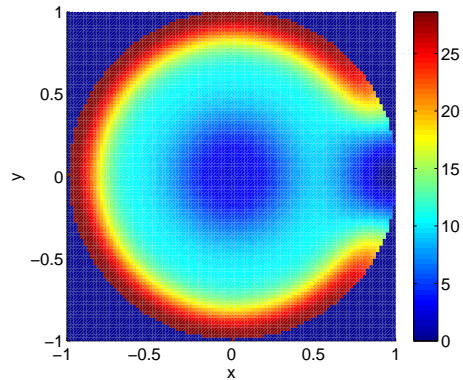


FIG. 6: (color online) Correlation plot $g(\mathbf{r}, \mathbf{r}')$ for $N = 9$ particles and $\alpha = 2$, corresponding to Fig. 4. The position \mathbf{r}' is fixed at $(0.95, 0)$, and the color scale indicates the correlation degree for different \mathbf{r} within the quantum dot.

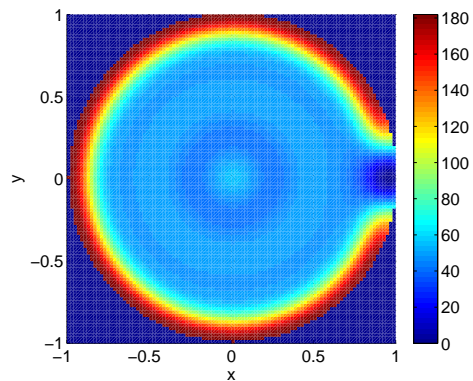


FIG. 7: (color online) Same as Fig. 6 but for $N = 19$.

A first possible configuration has all particles arranged equidistantly on a unit circle, resulting in the classical energy

$$E_c^{(1)}(N) = \frac{N\alpha}{2} \times \begin{cases} \sum_{k=1}^{(N-1)/2} \frac{1}{\sin(\pi k/N)}, & N \text{ odd,} \\ \sum_{k=1}^{(N-2)/2} \frac{1}{\sin(\pi k/N)} + \frac{1}{2}, & N \text{ even.} \end{cases} \quad (15)$$

If instead one particle resides at the origin plus $N - 1$ particles on the outer ring as above, the energy of this second configuration is

$$E_c^{(2)}(N) = E_c^{(1)}(N - 1) + (N - 1)\alpha. \quad (16)$$

For $N \leq 16$, numerical minimization of Eq. (14) shows that these two configurations always yield the lowest-energy solutions. In particular, $E_c^{(1)} < E_c^{(2)}$ for $N < 12$, see Table I. For $16 < N \leq 20$, an additional inner ring is formed containing $N_1^{\text{cl}} > 1$ particles, surrounded by

N	N_1	N_2	N_3	N_1^{cl}	N_2^{cl}	N_3^{cl}
2	2	-	-	2	-	-
3	3	-	-	3	-	-
4	4	-	-	4	-	-
5	4	-	-	5	-	-
6	6	-	-	6	-	-
7	7	-	-	7	-	-
8	8	-	-	8	-	-
9	9	-	-	9	-	-
10	10	-	-	10	-	-
11	1	10	-	11	-	-
12	1	11	-	1	11	-
13	1	12	-	1	12	-
14	1	13	-	1	13	-
15	2	13	-	1	14	-
16	3	13	-	1	15	-
17	1	3	13	2	15	-
18	1	3	14	2	16	-
19	1	3	15	3	16	-
20	1	3	16	3	17	-

TABLE I: Shell filling sequence for a 2D interacting Dirac fermion dot with circular hard-wall confinement. N_i^{cl} denotes the number of particles in the i th spatial shell obtained from the minimization of the classical electrostatic energy [Eq. (14)]. N_i is the corresponding HF quantity for $\alpha = 2$, see main text.

the outer ring containing $N_2^{\text{cl}} = N - N_1^{\text{cl}}$ particles. For all $N \leq 20$, the classical lowest-energy solution thus has at most two spatial shells, but configurations with three shells as observed in the quantum calculation are energetically quite close. The agreement between the shell filling sequence observed for $\alpha = 2$ and in the classical limit is not perfect but indicates that we are already rather close to the classical limit for $\alpha = 2$ and have a Wigner molecule, despite of the theoretically predicted absence of Wigner crystallization in bulk graphene.³⁷ Even for $\alpha = 1$, the above density plots suggest that incipient Wigner molecule behavior can be observed. (Of course, this is a smooth crossover and not a phase transition.) However, the fact that there are still substantial quantum fluctuations for $\alpha = 2$ is also clear from the addition spectrum in Fig. 3. In the deep classical limit, there is much less pronounced structure in the addition energy spectrum.

Finally, we point out that there is also interesting spin texture in such a quantum dot. The Pauli matrices in Eq. (1) are directly connected to the electronic spin density in a topological insulator surface via the relation^{3,38}

$$\mathbf{s}(\mathbf{r}) = (s_x, s_y)^T = \frac{\hbar}{2} \langle \hat{e}_z \times \boldsymbol{\sigma} \rangle. \quad (17)$$

For the case of graphene, the Pauli matrices refer to the sublattice degree of freedom, which is not easily accessible to experiments. The spin density (17) points within the 2D plane and is always isotropic, i.e., independent of

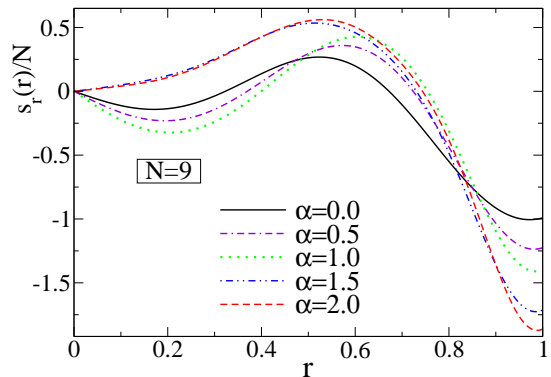


FIG. 8: (color online) HF results for the spin density s_r in radial direction vs r for $N = 9$ and various α .

the angular variable. We find that only the radial component $s_r(r) := \mathbf{s} \cdot \hat{e}_r$ (with $\hat{e}_r = \mathbf{r}/r$) does not vanish. The resulting nontrivial spin texture is shown in Fig. 8 for $N = 9$ and several α .

V. DISCUSSION

In this paper, we have discussed interaction effects in circular 2D quantum dots where the particles are massless Dirac fermions. Physical realizations of the studied model are given by graphene and the surface state of a topological insulator. For the case of two particles, we have compared three different methods to establish that Hartree-Fock calculations provide highly accurate results for physically relevant interaction strengths. An alternative method based on the Müller density matrix functional was also studied, but since Müller's *Ansatz* for the two-particle density respects the right normalization condition but sacrifices its positivity, it suffers from an unphysical divergence for sufficiently strong interactions. An improvement would have to take this drawback into account, while not dropping the sum rule for the density and the convexity of the functional.

The case of $N \leq 20$ particles has then been studied using Hartree-Fock simulations. The resulting addition spectrum of the quantum dot reveals pronounced magic numbers that cannot be explained by a noninteracting picture. Moreover, the density profiles and the density-density correlation functions show that we are rather close to the classical limit already for experimentally relevant interaction parameters ($\alpha \approx 1$ to 2). The formation of spatial shells is a clear signature of a Wigner molecule, and we therefore predict that in such a finite-size system the usual argument³⁷ for absence of Wigner crystallization of Dirac fermions can be effectively circumvented.

Acknowledgments

We acknowledge useful discussions with A. De Martino, W. Häusler, and E. Stockmeyer. This work was

supported by the Sonderforschungsbereich TR 12 of the DFG.

-
- ¹ A.K. Geim and K.S. Novoselov, *Nature Materials* **6**, 183 (2007).
- ² A.H. Castro Neto, F. Guinea, N.M.R. Peres, K.S. Novoselov, and A. Geim, *Rev. Mod. Phys.* **81**, 109 (2009).
- ³ M.Z. Hasan and C.L. Kane, *Rev. Mod. Phys.* **82**, 3045 (2010).
- ⁴ X.L. Qi and S.C. Zhang, arXiv:1008.2026.
- ⁵ N.P. Butch, K. Kirshenbaum, P. Syers, A.B. Sushkov, G.S. Jenkins, H.D. Drew, and J. Paglione, *Phys. Rev. B* **81**, 241301(R) (2010).
- ⁶ L.P. Kouwenhoven, D.G. Austing, and S. Tarucha, *Rep. Prog. Phys.* **64**, 701 (2001).
- ⁷ S.M. Reimann and M. Manninen, *Rev. Mod. Phys.* **74**, 1283 (2002).
- ⁸ N. Stander, B. Huard, and D. Goldhaber-Gordon, *Phys. Rev. Lett.* **102**, 026807 (2009); A.F. Young and P. Kim, *Nature Physics* **5**, 222 (2009).
- ⁹ J.M. Pereira, V. Mlinar, F.M. Peeters, and P. Vasilopoulos, *Phys. Rev. B* **74**, 045424 (2006).
- ¹⁰ P.G. Silvestrov and K.B. Efetov, *Phys. Rev. Lett.* **98**, 016802 (2007).
- ¹¹ H.Y. Chen, V. Apalkov, and T. Chakraborty, *Phys. Rev. Lett.* **98**, 186803 (2007).
- ¹² A. Matulis and F.M. Peeters, *Phys. Rev. B* **77**, 115423 (2008).
- ¹³ P. Recher, J. Nilsson, G. Burkard, and B. Trauzettel, *Phys. Rev. B* **79**, 085407 (2009).
- ¹⁴ M.V. Berry and R.J. Mondragon, *Proc. R. Soc. Lond. A* **412**, 53 (1987).
- ¹⁵ S. Schnez, K. Ensslin, M. Sigrist, and T. Ihn, *Phys. Rev. B* **78**, 195427 (2008).
- ¹⁶ J. Wurm, A. Rycerz, I. Adagideli, M. Wimmer, K. Richter, and H.U. Baranger, *Phys. Rev. Lett.* **102**, 056806 (2009).
- ¹⁷ A. De Martino, L. Dell’Anna, and R. Egger, *Phys. Rev. Lett.* **98**, 066802 (2007).
- ¹⁸ M. Ramezani Masir, A. Matulis, and F.M. Peeters, *Phys. Rev. B* **79**, 155451 (2009).
- ¹⁹ W. Häusler and R. Egger, *Phys. Rev. B* **80**, 161402(R) (2009).
- ²⁰ R. Egger, A. De Martino, H. Siedentop, and E. Stockmeyer, *J. Phys. A: Math. Theor.* **43**, 215202 (2010).
- ²¹ L.A. Ponomarenko, F. Schedin, M.I. Katsnelson, R. Yang, E.W. Hill, K.S. Novoselov, and A.K. Geim, *Science* **320**, 356 (2008).
- ²² C. Stampfer, J. Güttinger, F. Molitor, D. Graf, T. Ihn, and K. Ensslin, *Appl. Phys. Lett.* **92**, 012102 (2008).
- ²³ K. Todd, H.T. Chou, S. Amasha, and D. Goldhaber-Gordon, *Nano Lett.* **9**, 416 (2009).
- ²⁴ S. Schnez, F. Molitor, C. Stampfer, J. Güttinger, I. Shorubalko, T. Ihn, and K. Ensslin, *Appl. Phys. Lett.* **94**, 012107 (2009).
- ²⁵ J. Güttinger, C. Stampfer, F. Libisch, T. Frey, J. Burgdorfer, T. Ihn, and K. Ensslin, *Phys. Rev. Lett.* **103**, 046810 (2009).
- ²⁶ K.A. Ritter and J.W. Lyding, *Nature Materials* **8**, 235 (2009).
- ²⁷ A. Tarasov, S. Hugger, H. Xu, M. Cerchez, T. Heinzel, I.V. Zozoulenko, U. Gasser-Szerer, D. Reuter, and A.D. Wieck, *Phys. Rev. Lett.* **104**, 186801 (2010).
- ²⁸ G.E. Brown and D.G. Ravenhall, *Proc. R. Soc. London Ser. A* **208**, 552 (1951).
- ²⁹ J. Sucher, *Phys. Rev.* **107**, 1448 (1957); *Phys. Rev.* **109**, 1010 (1958); *Phys. Rev. A* **22**, 348 (1980); *Int. J. Quantum Chem.* **25**, 3 (1984).
- ³⁰ A.M.K. Müller, *Phys. Lett.* **105A**, 446 (1984).
- ³¹ R.L. Frank, E.H. Lieb, R. Seiringer, and H. Siedentop, *Phys. Rev. A* **76**, 052517 (2007).
- ³² B. Wunsch, T. Stauber, and F. Guinea, *Phys. Rev. B* **77**, 035316 (2008).
- ³³ M. Ezawa, *Phys. Rev. B* **77**, 155411 (2008).
- ³⁴ V.M. Bedanov and F.M. Peeters, *Phys. Rev. B* **49**, 2667 (1994).
- ³⁵ R. Egger, W. Häusler, C.H. Mak, and H. Grabert, *Phys. Rev. Lett.* **82**, 3320 (1999).
- ³⁶ C. Yannouleas and U. Landman, *Phys. Rev. Lett.* **82**, 5325 (1999).
- ³⁷ H.P. Dahal, Y.N. Joglekar, K.S. Bedell, and A.V. Balatsky, *Phys. Rev. B* **74**, 233405 (2006).
- ³⁸ A. Zazunov, A. Kundu, A. Hütten, and R. Egger, *Phys. Rev. B* **82**, 155431 (2010).
- ³⁹ T. Paananen and R. Egger, unpublished results.
- ⁴⁰ O. Gritsenko, K. Pernal, and E.J. Baerends, *J. Chem. Phys.* **122**, 204102 (2005).
- ⁴¹ E. Cancas and K. Pernal, *J. Chem. Phys.* **128**, 134108 (2008).
- ⁴² S. Walter, preprint arXiv:1010.6300.
- ⁴³ A. Bouzouina, *Proc. Roy. Soc. Edinburgh A* **132**, 1133 (2002).
- ⁴⁴ T. Maier and H. Siedentop, in preparation.